

The fate of river discharge on the continental shelf

1. Modeling the river plume and the inner shelf coastal current

Vassiliki H. Kourafalou¹

Rosenstiel School of Marine and Atmospheric Science, University of Miami, Miami, Florida

Lie-Yauw Oey

Atmospheric and Oceanic Science Program, Princeton University, Princeton, New Jersey

John D. Wang and Thomas N. Lee

Rosenstiel School of Marine and Atmospheric Science, University of Miami, Miami, Florida

Abstract. We study the development and evolution of buoyant river plumes on the continental shelf. Our calculations are based on three-dimensional numerical simulations, where the river runoff is introduced as a volume of zero salinity water in the continuity equation and mixing is provided by the model's turbulence closure scheme and wind forcing. In the absence of wind forcing the modeled river plumes typically consist of an offshore bulge and a coastal current in the direction of Kelvin wave propagation. We propose a plume classification scheme based on a bulk Richardson number, which expresses the relative magnitude of the buoyancy-induced stratification versus the available mixing. When the ratio of the discharge and shear velocities is greater (less) than 1, the plume is categorized as supercritical (subcritical); that is, the width of the bulge is greater (less) than the width of the coastal current. Supercritical plumes are often characterized by a meandering pattern along the coastal current, caused by a baroclinic instability process. For a given discharge, subcritical plumes are produced by large mixing and/or shallow water depths. In the presence of wind forcing the favorable conditions for offshore removal of coastal low-salinity waters include high river runoff and strong upwelling-favorable wind stress. When the rivers are treated as individual sources of freshwater ("point source" behavior), the wind-driven flow may exhibit substantial spatial variability. Under the above removal conditions, strong offshore transport takes place in "jetlike" flow regions within the river plume, in contrast to the downwind acceleration of adjacent waters. When the rivers are treated as a long "line source" of freshwater, the plume region resembles a coastal low-salinity band and the above removal conditions trigger offshore transport that is most pronounced at the "head" of the source.

1. Introduction

The coastal ocean is the recipient of freshwater and land-drained materials that are primarily brought in through river discharge. From the dynamical viewpoint the discharge site (the "river mouth") can be considered the source for both momentum and buoyancy, produced by the release of light fluid into a heavier (more dense) ambient. The resulting dynamical structure is referred to as a (buoyant) river plume. The present study is motivated by the need to understand and predict the phenomena that control the fate of riverine waters and related materials after

their release in the coastal ocean. Our main objective is to describe the generation and evolution of a river plume on the continental shelf and determine the important factors that govern its offshore expansion and, consequently, the removal mechanism of river-borne materials.

The frontal structure of a river plume has been discussed by several investigators. Earlier studies, such as those by *Kao et al.* [1977], *Kao* [1981], *Ikeda* [1984], and *Csanady* [1984], recognized the importance of nonlinearity, Coriolis, and friction in the development of the buoyant plume. *McClimans* [1986] identified the following three major processes that characterize the dynamics of the seaward expansion of the river flow: (1) acceleration, resulting from the balance between inertia and gravity (buoyancy) forces; (2) mixing, governed by turbulence due to bottom and interfacial friction; and (3) geostrophy, where the balance between Coriolis and the developed cross-shore pressure gradient (due to "freshening" of coastal waters) generates an alongshore coastal current, which is scaled by the baroclinic radius of deformation and

¹ Now at Consiglio Nazionale delle Ricerche, Istituto per lo Studio delle Metodologie Geofisiche Ambientali, Modena, Italy.

propagates leaving the coast to the right (left) in the northern (southern) hemisphere.

Chao and Boicourt [1986] applied a three-dimensional, primitive equation model to study the establishment of an estuarine plume by discharge of freshwater into the upper reaches of a model estuary adjacent to an enclosed basin. They found that 10 days of discharge were sufficient to establish a strong plume over the shelf, having many of the observed features, including an anticyclonic turning region and a subsequent southward coastal current. Garvine [1987] found a similar flow field by employing a reduced gravity model that allowed the outcropping of the density interface. He pointed out the strong nonlinearity of the plume dynamics and the role of rotation in forming the geostrophic coastal current. His results consisted of the steady state plume structure and, similar to Chao and Boicourt, were applicable to "strong" or "supercritical" plumes. The above results were extended by Chao [1988] for the cases of weak to moderate plumes.

Several studies addressed the generation and maintenance of a river plume and the related density-driven flow in conjunction with the influence of wind stress and/or other external forcings that are important in coastal circulation. Hickey and Hamilton [1980] used hydrographic data and a two-dimensional (2-D) baroclinic numerical model to simulate the distribution of density on the Washington and Oregon shelves. They modeled river discharge by a surface freshwater flux, and they found that the plume could become detached from the coast during periods of upwelling-favorable winds. This was also shown by Chao [1987] in a 3-D numerical study of the influence of suddenly imposed winds on riverine fronts and a verification through measurements of the Chesapeake plume was suggested. A similar finding for the South Atlantic Bight (SAB) coastal front was reported by Blanton *et al.* [1989], based on data from the Spring Removal Experiment (SPREX) and a two-dimensional, x - z (cross-shore, depth) numerical model that calculated offshore advection of lenses of low-salinity water during upwelling-favorable wind stress. They suggested that the observed mean southward flow in the nearshore region (opposite to the northeastward mean wind stress) was due to the freshening of the coastal waters. Analysis of data during a fall experiment on the SAB [Blanton *et al.*, 1994] revealed that the fall conditions on the shelf are characterized by vertical homogeneity, weak horizontal density gradients in the nearshore region (due to low river runoff), and a mean southward flow that is forced by the dominant downwelling-favorable winds.

In order to examine the dynamical processes that influence the transport of the nearshore, low-salinity waters of river origin on the continental shelf, we performed a series of numerical simulations. The strategy was to first analyze the physical mechanisms related to this transport and then represent them realistically enough to allow the employment of field observations for validation of the numerical results. The complexity and nonlinearity of the phenomena involved require a numerical model capable of accommodating the different forcings, which cover a wide range of timescales. We adopted the three-dimensional Blumberg and Mellor [1983] model, which is briefly described in the following section. In order to examine the model's response to buoyancy and winds, part 1 of this

two-part work involves process studies, where the model is forced externally by river discharge, first in the absence and then in the presence of wind stress; no tidal forcing is employed. Kourafalou *et al.* [this issue] (hereinafter referred to as part 2) deal with a realistic simulation of the circulation on the Southeast U.S. Continental Shelf during springtime, when the shelf receives maximum river runoff and realistic winds and tides are included. In both parts 1 and 2 we consider that the only cause of the coastal front is the difference between the salinity of the river and ocean water bodies, thus neglecting all temperature-related density gradients, as well as evaporative flux related salinity changes.

2. Model Description and Modifications

2.1. The Model

We use a 3-D, multilayer hydrodynamic model, which was initially developed by Blumberg and Mellor [1983]. The present application includes model modifications that are outlined here and further discussed by Oey and Chen [1992]. If \mathbf{u} is the horizontal velocity vector with components (u, v) and ∇ is the horizontal gradient operator, the model equations on an (x, y, z) Cartesian coordinate system are

$$\nabla \cdot \mathbf{u} + w_z = 0$$

$$\mathbf{u}_t + \mathbf{u} \cdot \nabla \mathbf{u} + w \mathbf{u}_z + f \mathbf{k} \times \mathbf{u} = -\nabla p / \rho_0 + (K \mathbf{u}_z)_z + \nabla(A \nabla \mathbf{u})$$

$$\rho g = -p_z \quad (1)$$

$$e_t + \mathbf{u} \cdot \nabla e + w e_z = (K e_z)_z + \nabla(A \nabla e)$$

$$\rho = \rho(T, S)$$

where w is vertical velocity; f is the Coriolis parameter; ρ_0 is a (constant) reference density; p and ρ are deviation pressure and density, respectively (i.e., the hydrostatic pressure p_0 associated with ρ_0 has been subtracted from the system); and e denotes either temperature T or salinity S . In part 1, the "f plane approximation" will be adopted, where a constant latitude ϕ is assumed for the calculation of the Coriolis parameter f ($f = 2\Omega \sin \phi$, where $\Omega = 7.292 \times 10^{-5} \text{ s}^{-1}$ and $\phi = 31^\circ$ for the SAB). The vertical eddy diffusivities of turbulent mixing for momentum K and heat and salt K_e are obtained through a second-order turbulence closure scheme ("level 2 1/2" turbulent closure model [Mellor and Yamada, 1982]).

The parameter A denotes both the horizontal viscosity and diffusivity coefficient and is parameterized using the Smagorinsky diffusion formula

$$A = C_a \Delta x \Delta y \left\{ u_x^2 + v_y^2 + 0.5(u_y + v_x) \right\}^{1/2} \quad (2)$$

where Δx , Δy is the horizontal grid size, C_a is a constant taken to be 0.2, and typical values of A on the continental shelf are 10 – $100 \text{ m}^2 \text{ s}^{-1}$.

A simple equation of state is used in the present study and is similar to Mamayev [1975] and Wang [1984]:

$$\sigma_t = 28.152 - 0.0735T - 0.00469T^2 + (0.802 - 0.002T)(S - 35) \quad (3)$$

where $\rho = 1 + \sigma_t \times 10^{-3} \text{ g cm}^{-3}$. The equation for temperature was not solved, since temperature was prescribed and kept at a constant value ($T = 18^\circ\text{C}$).

The model uses a σ - coordinate system, and the equations are solved with a second-order, leapfrog in time and central difference in space finite difference scheme. The σ - coordinate system is particularly suitable for coastal regions, where bathymetric effects are important. The method of solution uses a C - grid and the time differencing is explicit in the horizontal and implicit in the vertical. This removes time step constraints due to sigma vertical grid spacing. The horizontal grid spacing (5 km by 5 km here and in part 2) sets the time step constraints based on the Courant-Friedrichs-Lewy (CFL) criterion. The mode-splitting technique is adopted with a two-dimensional, external mode, short time step based on the (fastest) free-surface gravity wave speed and a three-dimensional, internal mode long time step based on the slower baroclinic wave speed. For the realistic SAB domain calculations (see section 4 and Kourafalou *et al.* [this issue]) the external time step was 20 s, the internal time step was 10 min, and simulations on the National Center for Atmospheric Research CRAY Y-MP required 9 MW of memory and 1 hour computer time for 50 days of integration.

The details of the model equations and method of solution are given by Blumberg and Mellor [1983]. The boundary conditions and the model modifications that were employed during the present study are outlined below.

2.2. Boundary Conditions

2.2.1. Wall boundaries. The normal and tangential velocities are zero at the sidewalls. At the ocean floor, salt flux is zero while momentum flux is balanced by quadratic bottom stress computed using the velocity \mathbf{u}_b nearest the bottom:

$$\begin{aligned} (K_s S)_z &= 0 \\ (Ku)_z &= C_D |\mathbf{u}_b| \mathbf{u}_b \end{aligned} \quad (4)$$

where K_s and K are the eddy viscosity coefficients for salt and momentum, respectively, and C_D is the bottom friction coefficient. For the box model experiments (section 3), C_D was set to a constant value ($C_D = C_{D\min} = 2.5 \times 10^{-3}$). When the realistic SAB model domain was employed (section 4 and Kourafalou *et al.* [this issue]), C_D was calculated by the logarithmic law of the wall and $C_{D\min}$ was used as a lower limit for the ratio

$$\frac{\kappa^2}{\ln^2 \left(\frac{z_b}{z_0} \right)} \quad (5)$$

where $\kappa=0.4$ (von Karman's constant), z_b is the distance from the bottom to the center of the lower layer, and z_0 is the roughness height. Physical considerations in choosing the value of z_0 include the type of bottom sediments ("roughness") and the height of bottom "ripples." A realistic estimate, however, is very hard to obtain, since bottom roughness is a highly variable quantity both in space and time ("measured" values of z_0 range from millimeters to tens of centimeters). The above expression

for C_D also suggests a mathematical constraint, so that z_b/z_0 would not be 1; this could happen in very shallow water, if vertical resolution is high. It is therefore recommended that different values of z_0 be assigned at different depths and for different study areas. For the purposes of this study the nearshore part of the shelf model area was given z_0 of the order of 1 cm.

2.2.2. Open boundaries. A modified Sommerfeld type radiation condition, used by Oey and Mellor [1993], was adapted for elevation, internal velocities, and the normal component of the external velocity. The radiation conditions are similar to Orlanski's [1976] with damping and forcing terms:

$$U_t + cU_n = \frac{U_F - U}{T_1} \quad (6)$$

where U denotes variable; n is the outward normal; $c = (gH)^{1/2}$ for the external mode and changed to the internal wave phase speed c_i for the internal mode; U_F is the forcing; T_1 is a timescale taken to be 3 hours, which corresponds to a "friction coefficient" of the order of 10^{-4} s^{-1} for the external mode, while increased by a factor of $(c/c_i)^{1/2}$ for the internal mode. For the tangential external velocities a free-slip condition was used.

For the idealized "box" model basin (section 3), dissipative layers were specified near the open boundaries, so that waves generated in the interior would be first partially absorbed and then radiated out at the boundary. This was achieved by slightly telescoping the grid near the north and east boundaries and by smoothly increasing the value of the horizontal eddy viscosity-diffusivity A there. Maximum values of A at the boundaries were thus in the range of 100 to $200 \text{ m}^2 \text{ s}^{-1}$ (for constant interior values of A during different experiments in the range of 10 to $200 \text{ m}^2 \text{ s}^{-1}$, see section 3). For the realistic SAB model domain (section 4 and Kourafalou *et al.* [this issue]), no telescoping or dissipative layers were employed near the boundaries and A was calculated by the Smagorinsky formula given above.

2.3. Freshwater Source

We implemented a freshwater source in the model's continuity equation. The river discharge is thus modeled as a volume of zero salinity water in the form of a coastal "mound" and is introduced at one or several coastal nodes (depending on the width of the "river") of the top model layer. The value of the coastal salinity in the immediate vicinity of the source is then determined by the model's mixing. This approach was pursued for two reasons. First, it allows a closed boundary along the coast everywhere, even at the river mouths. Consequently, there is no need to prescribe open boundary conditions at the coast, which would require a prescribed value of coastal salinity. When the river discharge is allowed to vary in time and when transient forcings, such as wind and tides, are considered, it is not possible a priori to specify salinity at the river mouth. Second, for a realistic simulation of river influx it is preferable to control the freshening of coastal waters through the amount of river discharge, which is readily available from river gauge measurements. The employment of a freshwater source allows time-dependent river discharge input. An outline of the numerical implementation of a

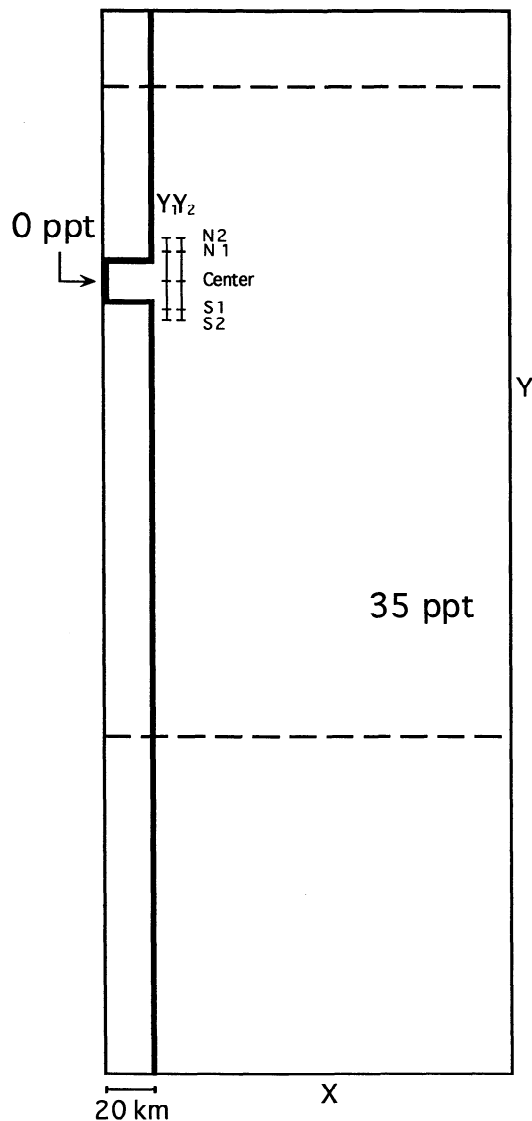


Figure 1. Box model basin, initially filled with water at 35 ppt. Freshwater (0 ppt) is introduced at the entrance of the river channel. The horizontal grid is 5 km by 5 km.

volume source in the model's conservation of mass equations is given in the appendix.

3. Process Studies on Buoyancy Forcing (Box Model)

In order to model the processes that influence the development and evolution of a river plume in the absence of wind and tidal forcing, a rectangular basin was adopted. The "box model" has characteristic SAB shelf dimensions as follows: approximately 200 km cross shore and 500 km alongshore (Figure 1). The horizontal grid spacing is 5 km by 5 km, and 11 layers are used in the vertical. The coast (thick solid line) is closed everywhere, and it geographically corresponds to the shelf's western boundary. Since the dynamical role of the river discharge is of primary interest in the inner shelf (coast to 20 m depth), the constant basin depth h experiments adopted $h \leq 20$ m. When cross-shore bottom slope was included, the box

model depth range was of the order of 100 m. For the initial condition the basin water was at rest, with a specified salinity of 35 parts per thousand (ppt). Then, water of zero salinity (river discharge) was applied at the coast at the head of a small channel (20 km long and 15 km wide). The channel constituted a crude representation of the river (or the river's estuary), and it was employed mainly for the needs of analytical calculations (see, for instance, the discharge velocity u_F that is calculated in section 3.2). The establishment of realistic estuarine flow, which would require a larger channel, is beyond the interests of the present study. Therefore the process studies that follow are based on the flow at the channel's (or river's) mouth and beyond at the connected ocean basin. The dashed lines in Figure 1 mark a model subregion that will be employed to improve the clarity of plotted results in this section.

3.1. Modeling the Development of the Plume and Coastal Current System

In order to emphasize both the offshore bulge and the coastal current, we adopted the term "plume and coastal current system" to describe the buoyancy-generated flow, although, for simplicity, we often use the term "plume" as an abbreviation for the system. The process studies that follow are based on different combinations of model parameters that we found most influential in determining the "shape" of the plumes. These parameters are the horizontal eddy viscosity/diffusivity A , the vertical eddy viscosity/diffusivity K , the freshwater discharge rate Q , and the depth of the receiving basin h . Since K is variable, its value was estimated as a spatial average near the river mouth. Also, the vertical salinity gradient ΔS was calculated as the difference between the near-top and near-bottom salinity in the basin near the river's mouth.

The offshore boundary of the computed plumes is marked by the 34 ppt isohaline. We define L as the seaward extent of the bulge (taken as cross-shore distance from the channel mouth to the plume boundary) and L_c as coastal current width (taken as distance from the coast to the plume boundary across the "head" of the coastal current, where southward velocity is maximum). After an initial adjustment of about 10-20 days, both L and L_c ceased to exhibit significant changes. At this stage we will call the plume "fully developed" and we will employ the ratio $\lambda = L/L_c$ to characterize the plume's shape. The nomenclature we adopted has been discussed by Chao [1988] and distinguishes among supercritical and subcritical plume types (here taken as $\lambda > 1$ and $\lambda < 1$, respectively). When λ is close to 1, the plume exhibits "diffusive" behavior; that is, the bulge and coastal current regions have merged ($L \approx L_c$) and the plume dissipates energy in the offshore direction.

In the next section we describe representative experiments, which are summarized in Table 1. Several more experiments were carried out, and they are described by Kourafalou [1993]. The cases presented herein include all the major findings of our process studies.

3.1.1. Control run (test 1). The following parameters were chosen as characteristic for modeling the development of a riverine buoyant plume in the inner shelf: $A=40 \text{ m}^2 \text{ s}^{-1}$, $Q=800 \text{ m}^3 \text{ s}^{-1}$, and $h=20$ m; the

Table 1. Box Model Test Cases and Types of Plumes

Test Case	h , m	Q , m^3s^{-1}	A , m^2s^{-1}	K , 10^{-2} m^2s^{-1}	ΔS , ppt	u_* , cm s^{-1}	u_F , cm s^{-1}	u_D , cm s^{-1}	R ,	F ,	λ	Type
1	20	800	40	1.0	7	3	18	33	6.0	0.5	4.3	a
2.1	20	800	75	1.0	7	3	18	33	6.0	0.5	3.0	a
2.2	20	800	100	2.0	11	5	21	41	4.2	0.5	2.8	a
2.3	20	800	200	2.0	11	5	21	41	4.2	0.5	1.3	a
3.1	20	800	40	2.0	5	5	16	28	3.2	0.6	4.0	a
3.2	20	800	40	5.0	3	13	13	21	1.0	0.6	0.8	b
4.1	20	1600	40	2.0	10	5	25	39	5.0	0.6	4.7	a
4.2	20	3200	40	2.0	9	5	31	36	6.2	0.9	5.5	a
4.3	20	200	40	0.5	3	1	8	21	8.0	0.4	6.0	a
5.1	5	800	40	5.0	5	50	16	14	0.3	1.1	0.5	b
5.2	5	1600	40	5.0	8	50	23	18	0.5	1.3	0.7	b
5.3	5	800	40	10.0	4	100	15	13	0.2	1.1	0.9	b

Variables are defined as follows: h , constant basin depth; Q , freshwater discharge rate; A , eddy viscosity/diffusivity; K , vertical eddy viscosity/diffusivity; ΔS , vertical salinity gradient; u_* , shear velocity; u_F , velocity of discharged freshwater; u_D , densimetric velocity; R and F , nondimensional quantities used to characterize the shape of plumes; and λ , characteristic length. Type a is supercritical and b is subcritical.

computed K was of the order of $100 \text{ cm}^2 \text{ s}^{-1}$. The surface salinity and velocity fields after 40 days of integration are presented in Figure 2. It is clear that the bulge ($L=65 \text{ km}$) is much wider than the coastal current ($L_c=15 \text{ km}$), which characterizes the plume as supercritical ($\lambda > 1$). Maximum velocities reached about $15\text{--}18 \text{ cm s}^{-1}$ in the bulge and $8\text{--}10 \text{ cm s}^{-1}$ in the coastal current, while ΔS was 7 ppt.

Examination of the corresponding fields at $t=20$ days and at $t=60$ days (not shown) revealed the following. A "secondary bulge" formed at $t=20$ days southward of the

main bulge and was well established by $t=40$ days (Figure 2), when a third bulge farther south started to appear. The offshore expansion of the main bulge ceased at around 40 days, while the secondary bulge expanded until about 60 days and the third bulge was also slowly gaining in size. The coastal current thus exhibited a "meandering" pattern. Most other analytical and numerical plume studies in the literature present a unidirectional rather than meandering coastal current. Figure 2 shows an alongshore separation between meander "peaks" of about 60 km (hence is not due

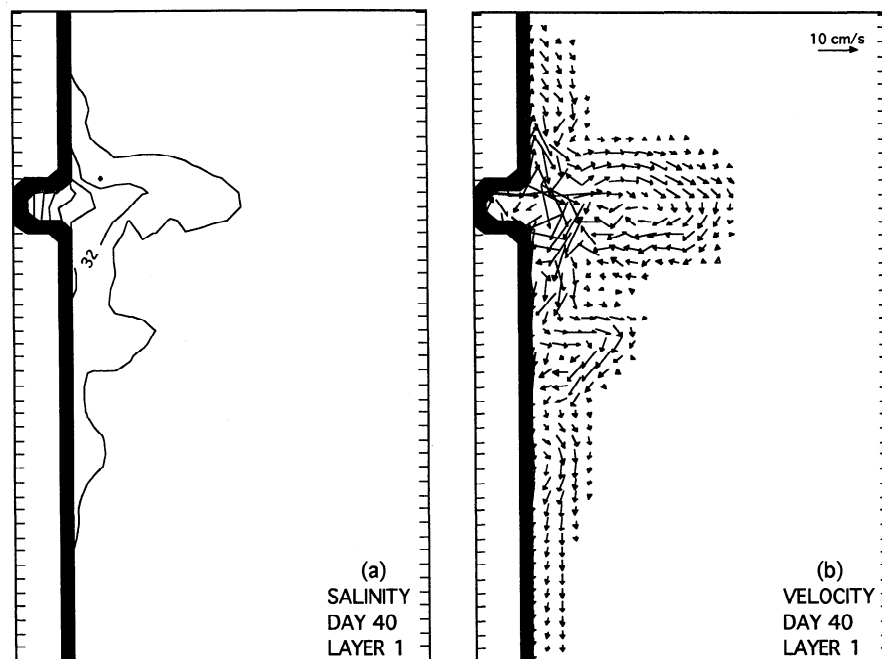


Figure 2. Model-computed, near-surface (a) salinity and (b) velocity fields for day 40 of the control run (test 1); salinity contour interval is 2 ppt.

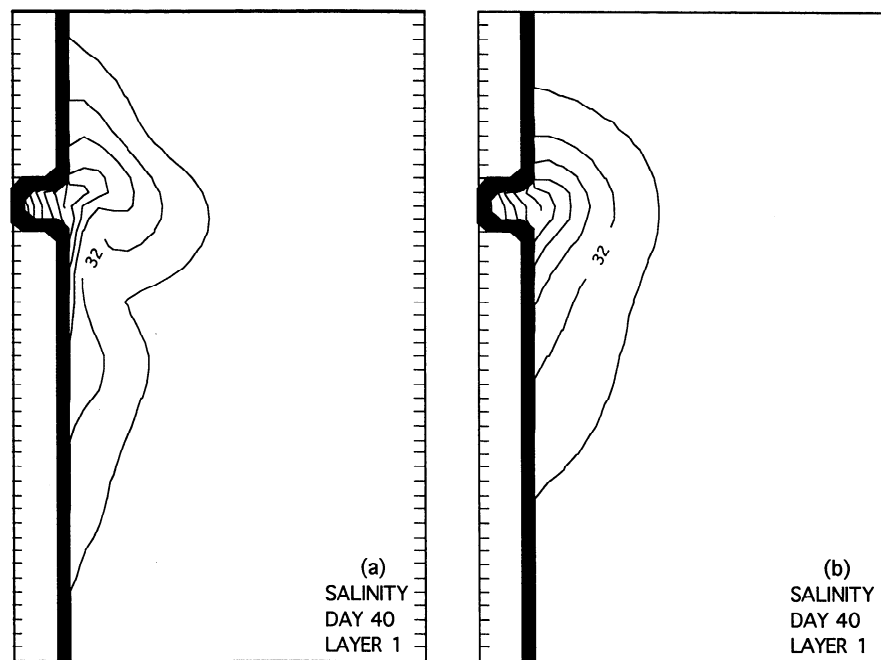


Figure 3. Model-computed, near-surface salinity (contour interval is 2 ppt) at day 40 and for different coefficients of eddy viscosity A (test 2); (a) $A=100 \text{ m}^2 \text{ s}^{-1}$ (test 2.2) and (b) $A=200 \text{ m}^2 \text{ s}^{-1}$ (test 2.3).

to numerical $2\Delta y$ noise) and a meander width of about 10–30 km. Since the present numerical simulation excludes forcing mechanisms and mixing agents, such as wind and tides, which presumably would eliminate the meandering pattern, it is very difficult to isolate and distinguish its origin based on observations. As in the work by *Oey and Mellor* [1993], the coastal current meander is caused by a baroclinic instability process (see section 3.2).

3.1.2. Variable horizontal eddy viscosity/diffusivity (test 2). Experiments similar to the control run were performed with different values for A . The test cases 2.1 to 2.3 refer to $A=75$, 100, and $200 \text{ m}^2 \text{ s}^{-1}$. The plume stayed supercritical up to $A=100 \text{ m}^2 \text{ s}^{-1}$ (Figure 3a) and became "diffusive" for higher values; λ was thus greater or close to 1 in all test 2 cases. As A increased, the meandering of the coastal current was diminished, while the southward extent of the plume (taken at $t=40$ days) increased and reached a maximum of 150 km at $A=75 \text{ m}^2 \text{ s}^{-1}$. For higher values of A , however, no distinct coastal current was observed, λ was close to 1, and the plume expanded mainly in the offshore direction; case 2.3, for instance (Figure 3b), exhibits a reduced southward extension of 90 km.

3.1.3. Variable vertical eddy viscosity/diffusivity (test 3). We increased the effective value of K through the value of a "background" mixing model parameter. All test 3 cases involved K larger than what was calculated by the turbulence closure scheme in the control run. As K increased, the plume became slower in lateral expansion and deepened. For moderate increase in K the plume remained supercritical (Figure 4a, test 3.1; $L=40$ km, $L_c=10$ km, $\lambda>1$), but ΔS was reduced. Further increase in K , however, resulted in subcritical plume (test 3.2, Figure 4b; $L=12$ km, $L_c=15$ km, $\lambda<1$). In all simulations with increased K the southward extension of

the plume was about 90 km at $t=40$ days and the meandering of the coastal current was reduced or eliminated.

3.1.4. Variable river discharge (test 4). Changes in the freshwater rate Q (not shown) did not alter the plume characteristics significantly. For $Q=1600 \text{ m}^3 \text{ s}^{-1}$ (test 4.1) the southward extent of the plume increased (as compared with the control run) to 170 km by $t=40$ days. For $Q=3200 \text{ m}^3 \text{ s}^{-1}$ (test 4.2) the plume almost reached the southward boundary of the basin by $t=20$ days; L was 85 km and L_c was 15 km. In both cases the plume was supercritical and the meandering of the coastal current was more pronounced than the $Q=800 \text{ m}^3 \text{ s}^{-1}$ control run case. For a low discharge rate of $Q=200 \text{ m}^3 \text{ s}^{-1}$ (test 4.3) the plume was still supercritical but slower in progress. At $t=40$ days the southward extent and ΔS were only 35 km and 3 ppt, respectively. By $t=60$ days a secondary bulge started to form, indicating the possibility of development of a meandering coastal current despite the low discharge conditions.

3.1.5. Variable basin depth (test 5). The depth of the flat model basin was reduced first to 10 and then to 5 m; the results with $h=10$ m were not very different than the $h=20$ m experiments and are not shown. Figure 5a gives the surface salinity field for $h=5$ m and $t=40$ days (test 5.1). The plume is subcritical, with less northward and offshore extent than in the control run simulation (compare with Figure 2a) but with a wider coastal current reaching 135 km down the coast. Further integration until $t=80$ days (not shown) revealed the same characteristics, with enhanced offshore and downshore extension and a tendency for diffusive state. A secondary bulge started forming by $t=20$ days, and a third bulge was apparent by $t=60$ days. The shallowness of the basin greatly increased vertical mixing. Consequently, the offshore extent of the bulge

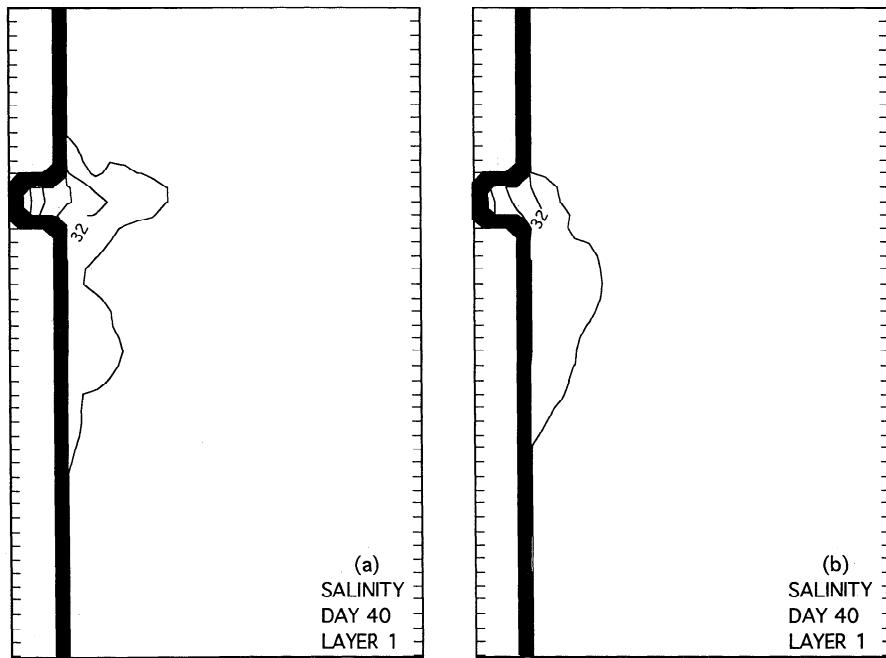


Figure 4. Same as Figure 3, but for variable vertical eddy viscosity coefficient K (test 3); (a) $K \sim 2 \times 10^{-2} \text{ m}^2 \text{ s}^{-1}$ (test 3.1) and (b) $K \sim 5 \times 10^{-2} \text{ m}^2 \text{ s}^{-1}$ (test 3.2).

was $L=20$ km only (almost a third of the width of the control run bulge). Comparison to the broad coastal current region ($L_c=40$ km) clearly determined a subcritical plume ($\lambda < 1$). Similar results were obtained for smaller A ($A=30 \text{ m}^2 \text{ s}^{-1}$, not shown) or higher Q in the 5 m basin. For instance, $Q=1600 \text{ m}^3 \text{ s}^{-1}$ (test case 5.2) gave $\lambda=0.7$, which was larger than the 5.1 case but still less than 1, so that the plume was again subcritical. When K was set to higher values, however, no distinct coastal current was

observed and λ was close to 1. An example is test case 5.3 (Figure 5b).

3.2. Discussion

3.2.1. Plume dynamics. As mentioned earlier, our experiments suggested that the value of λ did not alter significantly after about 10–20 days. The plumes that were described in the previous section were thus "fully developed." In order to discuss the early stages of plume

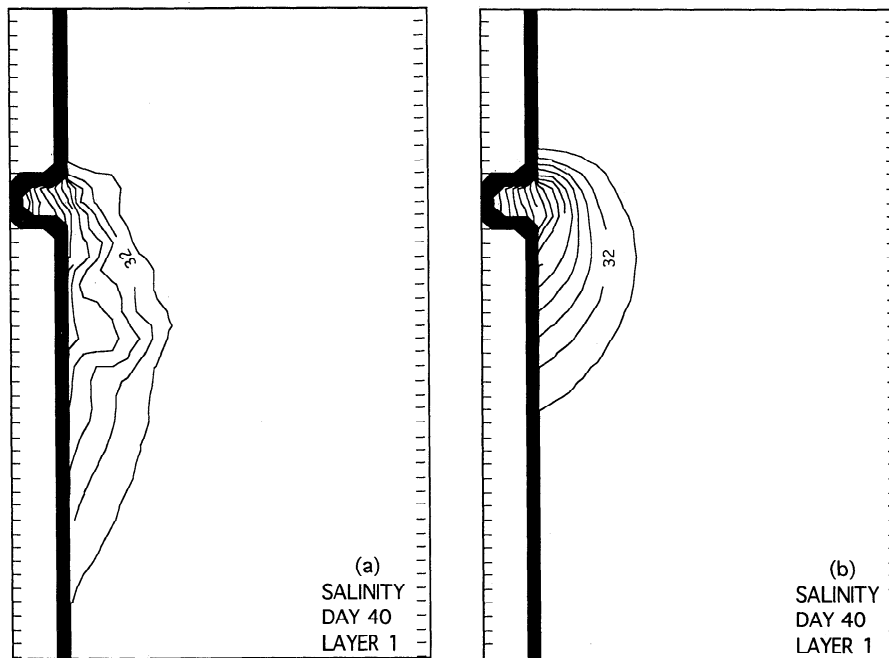


Figure 5. Same as Figure 3, but for basin depth $h=5$ m (test 5); (a) all parameters, same as for the control run (test 5.1.) and (b) increased vertical mixing (test 5.3).

Table 2a. River Plume Characteristics at $t=2$ Days and When the Coriolis Force Is Neglected

	u , cm s ⁻¹		v , cm s ⁻¹		S , ppt	
	Y1	Y2	Y1	Y2	Y1	Y2
<i>Near Top</i>						
N2	-0.3	-0.1	1.8	1.2	35.0	35.0
N1	2.3	0.6	9.8	5.2	34.1	34.8
Center	20.3	7.9	-0.9	-0.8	30.4	33.3
S1	2.4	0.6	-9.8	-5.2	34.1	34.1
S2	-0.3	-0.1	-1.8	-1.2	35.0	35.0
<i>Near Bottom</i>						
N2	-0.3	-0.1	-1.1	1.0	35.0	35.0
N1	-1.4	-0.3	-4.9	3.9	35.0	35.0
Center	-5.8	-1.4	1.0	-0.8	34.9	35.0
S1	-1.4	-0.3	4.9	-1.0	35.0	35.0
S2	-0.3	-0.1	1.1	-0.4	35.0	35.0

u is cross-shore velocity (positive offshore), v is alongshore velocity (positive northward) and S is salinity. Y1 and Y2 are alongshore segments (first and second nearest to the source). Cross-shore locations are at the first and second nodes north of the source (N1 and N2), at the center of the sources, and at the first and second nodes south of the source (S1 and S2), see Figure 1.

development, we examine velocity and salinity values after 2 days of simulation and along the sections Y_1 , Y_2 (Figure 1). The following two cases are considered: (1) conditions identical to the control run (Table 2a) and (2) same as in the control run but with the Coriolis force model term set to zero (Table 2b).

The tabulated values reveal the following. In both cases the surface u velocity is highest near the source, decreasing offshore, and the deeper cross-shore velocity fields are generally of opposite sign. The surface v velocity is symmetric around the source in the nonrotating case, while it has a weak northward and a strong southward component in the rotating case. The southward current has a weak counterflow in the deeper layer. Salinity values show the location of the lowest salinity in the rotating case near the coast and immediately south of the river's mouth. When rotation is ignored, the lowest salinity is found in front of the discharge site (source's center). The vertical motion (not shown) was upward at the center of the source and generally downward at the periphery of the plume in both experiments. This indicates that upward transfer of mass takes place near the mouth, where the surface offshore transport is strongest, while some plume water sinks around the frontal boundary, presumably due to the convergence of the surface flow there.

It is evident that the Coriolis force is responsible for the "asymmetry" in both velocity and salinity fields. To illustrate the consequences of this asymmetry in the development of the plume and coastal current system, we refer to the fully developed plume in Figure 2. Three distinct flow regimes have been established as follows: north regime (nearshore area north of the channel's mouth), east regime (in front and seaward of the channel's mouth),

Table 2b. River Plume Characteristics at $t=2$ Days and When the Coriolis Force Is Included

	u , cm s ⁻¹		v , cm s ⁻¹		S , ppt	
	Y1	Y2	Y1	Y2	Y1	Y2
<i>Near Top</i>						
N2	-0.5	-0.1	0.1	0.1	35.0	35.0
N1	0.9	0.1	0.3	0.3	35.0	35.0
Center	10.9	2.2	3.6	0.4	34.7	35.0
S1	-3.4	0.3	-21.4	-3.6	29.9	34.1
S2	-0.3	0.9	-5.9	-1.2	33.4	35.0
<i>Near Bottom</i>						
N2	-0.1	-0.1	0.0	0.1	35.0	35.0
N1	-0.1	-0.1	0.1	0.3	35.0	35.0
Center	-0.7	-0.2	0.5	1.1	34.9	35.0
S1	2.1	0.4	7.6	0.7	35.0	35.0
S2	0.7	0.1	0.3	-0.6	35.0	35.0

See Table 2a description.

and south regime (nearshore area south of the channel's mouth). The upper layer flow within the three areas exhibits different characteristics.

In the east region the upper layer flow is maintained within the bulge of the plume and has a strong offshore component near the mouth, which is gradually weakened and turns onshore at the outer part of the bulge. The low salinity water that is released by the river is thus first advected offshore, then deflected to the right and back toward the coast by the Coriolis force. The onshore flow forms a "pool" of low-salinity waters immediately south of the river mouth.

The south regime exhibits the most prominent near-surface flow. It is shoreward within the low-salinity pool and is followed by a distinct southward current which occupies a narrow portion of the nearshore area. This southward flow is the "coastal current" that results from the geostrophic adjustment of the flow to the pressure gradient that is primarily due to the density difference between the riverine and the ambient waters.

The upper layer flow in the north region is relatively weak as compared with the east and south regimes and directed northward by the coast and southward (toward the bulge of the plume) farther offshore due to the Coriolis effect. It is confined within a narrow nearshore area and is due to the pressure gradient between low-salinity waters near the mouth and ambient waters immediately north. This alongshore gradient cannot be balanced geostrophically by cross-shore flow, which is zero in the vicinity of the coast. The northward extent of this flow is also retarded by both friction and the Coriolis-induced, anticyclonic turn toward the main core of the plume.

The flow within the plume exhibits nonlinear behavior. The bulge and coastal current regions are connected through a nearshore area of strong cyclonic flow, apparently due to the shoreward movement of the low-salinity water there. Our findings thus reveal the importance of the nonlinear and Coriolis terms in the development of a midlatitude plume and coastal current system [Chao and Boicourt,

1986; Garvine, 1987; Chao, 1988]. We detect that it is the momentum balance between these terms that causes the turning of the flow from the bulge toward the coast. The consequent concentration of low-salinity water immediately south of the mouth increases the offshore pressure gradient there and is the cause of the geostrophic southward current. Linear models [e.g., Ikeda, 1984; Csanady, 1984] show a fanlike distribution of streamlines (and similarly for salinity lines) that bend offshore and shoreward. The most significant consequence of the absence of a bulge is the resulting absence of the coastal current.

Garvine [1987] showed that the Coriolis effect is small when $k < 1$, where the Kelvin number k expresses the ratio of a geometric length scale L that characterizes the horizontal extension of the plume to the baroclinic Rossby radius of deformation r :

$$k = \frac{L}{r}. \quad (7)$$

For the circulation within the estuary, L is usually taken equal to the channel width. For the plume dynamics in the basin we infer that L is best represented by the cross-shore width of the plume next to the channel mouth and it coincides with the scale that we employed in section 3.1. Typical values of r reach a few kilometers. For the major rivers at the SAB continental shelf, k is close to 1 and the effect of the Earth's rotation cannot be neglected.

An important finding of our experiments was the "meandering" of the coastal current. This result agrees with the numerical study on riverine buoyant plumes by Oey and Mellor [1993]. Their model was similar to ours (sections 2.1 and 2.2) but with the low-salinity input introduced through a channel connecting the ocean basin (flat bottom at 20 m) to a "storage basin" that received the freshwater. They concluded that the meandering of the

coastal current had two stages of development, (1) a barotropic instability stage characterized by short wavelengths (≈ 20 km) and (2) a baroclinic instability stage characterized by long wavelengths (≈ 60 km). Our results presented meanders of large wavelengths (see, for instance, Figure 2, where the meander wavelength is about 60 km), indicating that baroclinic instability is dominant. We conclude that our model result is robust, since meanders are produced independent of the way that the freshwater is specified. We further showed that the meandering was enhanced with increased buoyancy and reduced or eliminated with increased mixing.

To assess the sensitivity of the results to grid resolution, the horizontal grid size was decreased from 5 to 3 km. We repeated several of the experiments on the finer grid, and we did not observe any significant changes in the produced plumes. Since the finer grid allowed the employment of smaller values for A , however, we performed tests with A reduced to 20 and $10 \text{ m}^2 \text{ s}^{-1}$. As A decreased, the coastal current meandering became more pronounced. When Q was increased (Figure 6a), the meandering was enhanced, but if K was increased (Figure 6b), the meandering vanished. These results are the same as those for the 5 km resolution. A model sensitivity test on the vertical resolution was also performed; a reduction in vertical resolution from 11 to 9, 7, and 5 layers revealed that for 20 m depth the minimum number of layers should be 7. Finally, tests with enhanced bottom friction produced effects similar to increase in vertical mixing; the coastal current ceased to meander or even disappeared as a distinct plume region.

3.2.2. Derivation of a plume classification scheme. A classification scheme that would characterize the above experiments and also represent the dynamic processes that determine the development of a buoyant

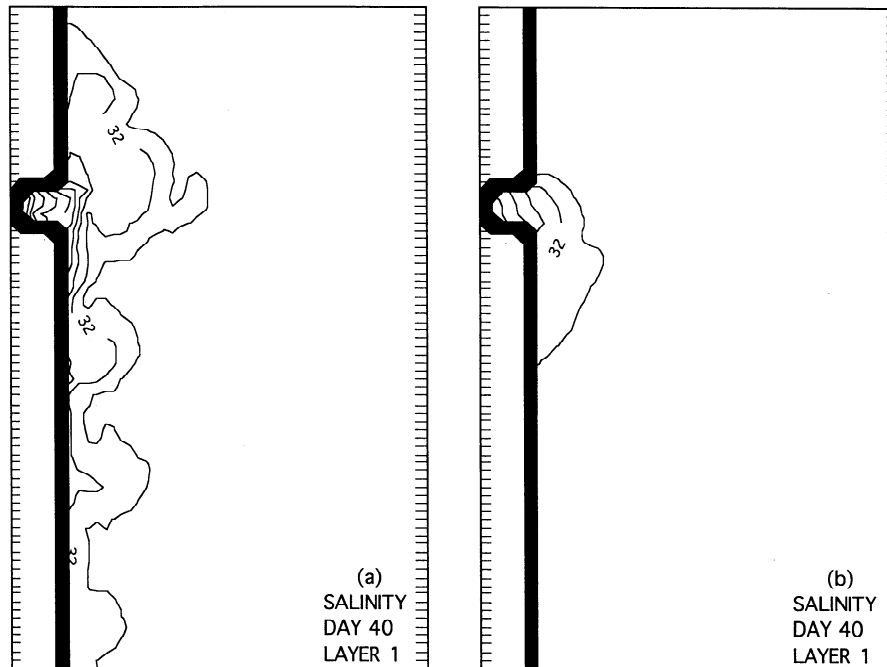


Figure 6. Same as Figure 3, but for 3 km by 3 km horizontal grid size; (a) $Q=1600 \text{ m}^3 \text{ s}^{-1}$, and $A=20 \text{ m}^2 \text{ s}^{-1}$; (b) $K=10 \times 10^{-2} \text{ m}^2 \text{ s}^{-1}$.

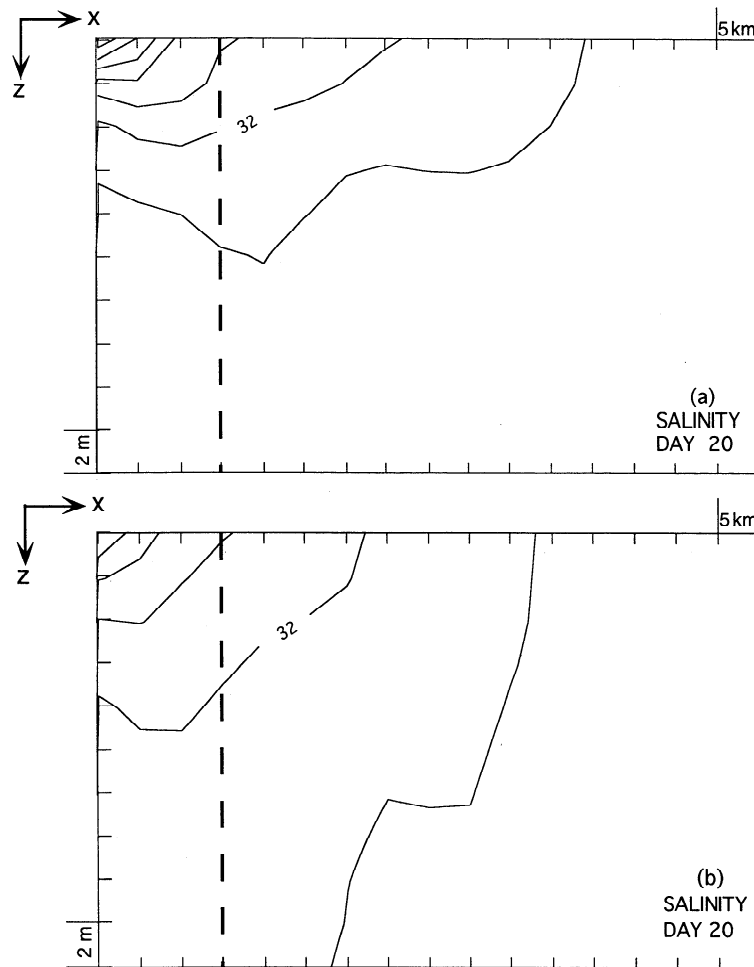


Figure 7. Model-computed vertical cross sections of salinity (contour interval is 2 ppt) across the plume's bulge at day 20 for (a) control run and (b) increased vertical mixing. Total depth is 20 m. The vertical dashed line is located at the channel mouth, where ΔS is computed.

plume on a rotating, constant-depth basin is derived herein. Gill [1977] and Garvine [1981, 1987] emphasized the initial stage of the plume development and adopted the supercritical/subcritical flow characterization that is defined with $F > 1$ and $F < 1$, respectively, where F is the densimetric Froude number:

$$F = \frac{U}{C}. \quad (8)$$

F expresses the ratio of the discharge speed to the celerity of long internal waves. Since U depends on the width of the channel, F is considered to impose a hydraulic type of control on the flow during the acceleration phase of plume development (see section 1). We suggest that in the event of a realistic estuarine channel with variable width, the flow could undergo transitions between the two stages, before its release to the ocean. The modeling of estuarine dynamics is beyond the scope of this study. We will therefore derive a characterization of the status of the flow in the coastal riverine plume and for the fully developed stage.

Chao [1988] extended the above Froude number concept to describe supercritical and subcritical coastal plumes according to the ratio of the width of the bulge L to the

width of the coastal current L_c . The plume was characterized as supercritical if $L > L_c$ and subcritical if $L < L_c$. Although our results present a feature that was absent in Chao's calculations, namely, the meandering of the coastal current, we also found that the ratio $\lambda = L/L_c$ is appropriate to characterize the different types of plumes. Furthermore, our simulations suggest that a more suitable parameter is the Richardson number Ri , since this measures the degree by which the available potential energy is dissipated by the currents it produces, or by the enhanced mixing we specify in the model. The different plumes that were described in section 3.1 can be indeed viewed as the products of the balance between the tendency for stratification due to the freshwater discharge and the tendency for homogeneity due to mixing. This becomes clear when vertical sections across the main bulge of the plumes are considered. The control run cross section (Figure 7a) resembles a two-layer system, while the test 3.1 plume (enhanced mixing conditions, Figure 7b) has a less stratified vertical structure near the mouth. For both F and Ri we sought expressions that are analytically compatible.

We chose the following three velocities as the important scales for the plume flow: the velocity of the discharged

freshwater u_F , the densimetric velocity u_D , and the shear velocity u_* . By argument of dimensional analysis [see *Kao, 1981*] the discharge velocity is defined as

$$u_F = (g' Q_F)^{1/3} \quad (9)$$

where g' is reduced gravity (gravity multiplied by the vertical density deficiency $\Delta\rho/\rho$ which is proportional to ΔS and Q_F is the amount of discharge Q divided by the channel width. For the densimetric velocity the celerity of the first baroclinic mode at the river's mouth was adopted [see *Chao, 1988*].

$$u_D = \frac{(g'h)^{1/2}}{\pi} \quad (10)$$

The model parameterization of bottom friction computes the shear velocity as proportional to the bottom layer velocity. Comparison of model computed K and u_* values gave the following analytical expression for u_* :

$$u_* = 50 \frac{K}{h} \quad (11)$$

This is similar to the semiempirical expression recommended by *Csanady [1976]* for shallow water.

According to the above, the densimetric Froude number is expressed as

$$F = \frac{u_F}{u_D} \quad (12)$$

For the Richardson number we follow *Fischer et al. [1979]*:

$$Ri = \frac{g' Q_F}{u_*^3} \quad (13)$$

and, according to our definition of u_F , we have

$$Ri = \left\langle \frac{u_F}{u_*} \right\rangle^3 \quad (14)$$

Thus another characteristic velocity ratio is defined as the third root of the Richardson number:

$$R = \frac{u_F}{u_*} \quad (15)$$

which we will call the river plume number. The two nondimensional quantities defined above, namely, R and F were found suitable to characterize the shape of plumes in the coastal ocean. *Hansen and Rattray [1965]* derived two bulk parameters physically similar to R and F to classify estuaries in terms of stratification and circulation.

The values of u_F , u_D , u_* , λ , R , and F are listed in Table 1 for all test cases. On the basis of the experiments presented herein, the following plume classification scheme is proposed: $R > 1$, supercritical plume; $R < 1$, subcritical plume; $R \approx 1$ and $F > 1$, supercritical plume; and $R \approx 1$ and $F < 1$, subcritical plume.

We emphasize that the above classification scheme is valid for fully developed buoyant plumes on a rotating, constant-depth basin. It should also be noted that the employed value of f (section 2.1) characterizes midlatitude

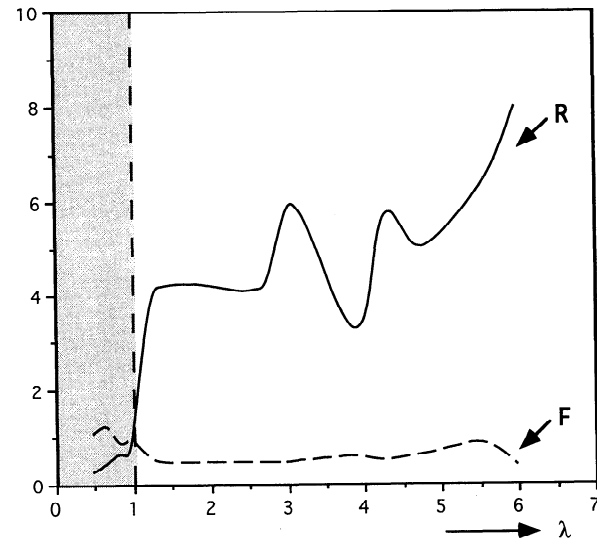


Figure 8. Plume number R (solid line) and Froude number F (dashed line) as a function of the characteristic plume length ratio λ . The shaded area covers the $\lambda < 1$ cases.

plumes. The experiments that computed λ close to 1 (diffusive plumes) correspond to high values of A or K . We speculate that the buoyancy-related available potential energy was diminished to the extent that no distinct coastal current was produced.

The values of R and F are plotted in Figure 8 over the characteristic length ratio λ . It is obvious that the Richardson-number-related ratio R offers a clear distinction between the $\lambda < 1$ and $\lambda > 1$ cases. We infer that this is due to the effects of dissipation that are described by R but not by F . The small values of R in the shaded area in Figure 8 ($\lambda < 1$), for instance, suggest that when frictional forces increase, the subcritical behavior prevails. Hence we have derived an easily measured, single parameter that offers a clear distinction between supercritical and subcritical plumes. *Chao [1988]* also found that dissipation had to be included in order to classify plume results. He first employed the Froude number, but he found that this parameter rarely exceeds 1. He then employed the coastal current intrusive speed C and compared the following two parameters: V/C_o , where V is the characteristic flow speed at the river mouth and C_o is the baroclinic phase speed, versus C/C_o . Although C is a measure of dissipation (it is small for large dissipation and vice versa), it is not easily observable and Chao's analysis did not offer a unique classification parameter.

3.2.3. The effect of bottom slope. The above experiments were repeated for several different cross-shore slopes. In all cases the channel and the first basin grid point had the same depth (with minimum depth set to 5 m). The computed plumes generally exhibited a bulge and slightly meandering coastal current. Figure 9a shows a salinity distribution that was typical for all slopes that started at 5 m. The slope in this particular incident was small, 2×10^{-4} (10 m depth at 50 km offshore, for instance). The computed salinity field, however, is very different than that of the flat bottom case (compare with

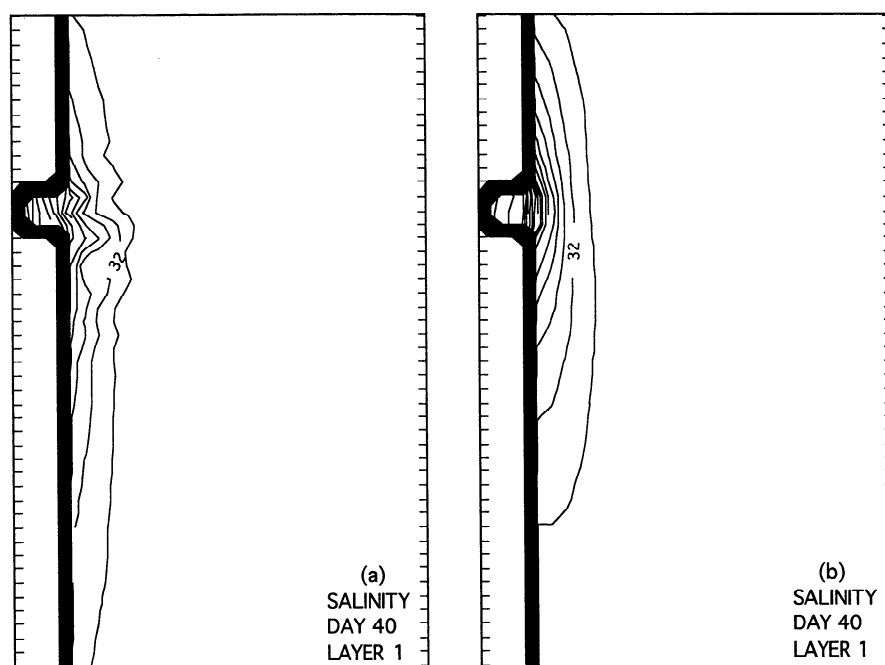


Figure 9. Same as Figure 5, but for sloping bottom.

Figure 5a). The offshore extent of the plume was reduced due to potential vorticity constraints. The flow stayed "coastally trapped," elongated in both northward and southward directions. When larger slopes were applied, the main difference was in the smaller width of the generated front. Our findings suggest that the presence of slope has a pronounced effect on the plume structure, while the magnitude of the slope is of secondary importance. The most apparent effect of sloping bottom is to restrict the offshore extension of the plume. However, if the slope becomes very large (larger than about 2×10^{-3}), the depth increases rapidly and the surface flow is isolated from the sloping bottom. The results are then similar to the flat bottom cases (supercritical plume in the absence of enhanced mixing). A slight increase in A or K in the presence of even a moderate slope was sufficient to produce a salinity field as in Figure 9b, where the bulge and coastal current areas have merged and no meandering is detected.

The effect of bottom slope on coastal trapping of both barotropic and baroclinic flows has been discussed in several studies. An example is *Chao's* [1988] employment of the vertically integrated vorticity equation for the "top" and "bottom" layers of the plume. He found that slope induced gain in anticyclonic vorticity for the plume due to enhanced upward motion and surface divergence. Indeed, comparison of our flat bottom versus small to moderate slope experiments revealed that slope caused upward movement, which created higher surface elevation near the river mouth. The increased northward (negative) pressure gradient enhanced the north extension of the plume, while the increased shoreward flow south of the mouth produced a stronger southward coastal current.

Although the plume classification scheme that was derived in the previous section was based on the flat bottom experiments, it can be employed to discuss sloping bottom results. *Chao* [1988] parameterized the effect of the

bottom slope on the discharge velocity u_F by multiplying u_F by a factor that is less than unity and that decreases as slope increases. This implies that slope encourages subcritical behavior, since reduction of u_F would make both R and F smaller and most possibly less than 1.

4. Process Studies on Wind Forcing (SAB Model)

4.1. The SAB Model Domain

As a first step toward a realistic SAB simulation (part 2), we adopt realistic geometry and bathymetry for the SAB continental shelf and study the responses to the combined buoyancy and wind stress inputs. The SAB model domain extends from approximately 27° N to 35° N and from 76° W to $81^\circ 30'$ W and is divided in a 5 km by 5 km horizontal grid (Figure 10), with nine vertical layers. The coastline was approximated as realistically as possible, and detailed bathymetry was prescribed. The dashed lines identify two different subregions, which will be used for presentation of model results as follows: region 1 for point source experiments (section 4.2) and region 2 for line source experiments (section 4.3). These subregions serve the same purpose as in section 3; that is, they will be used for plotting purposes only, bearing no influence on the model calculations.

As an initial condition, the shelf is quiescent and homogeneous, with salinity specified at 35 ppt. The model was forced at $t=0$ with constant river discharge Q , which was given typical springtime maximum values. For the wind stress a typical magnitude of 0.5 dyn cm^{-2} (corresponding to "moderate" wind speeds of about 5 m s^{-1}) was chosen. The applied wind stress vector was rotated from the model coordinate system (positive in the "true" north and east directions) to a local "alongshore"-"cross-

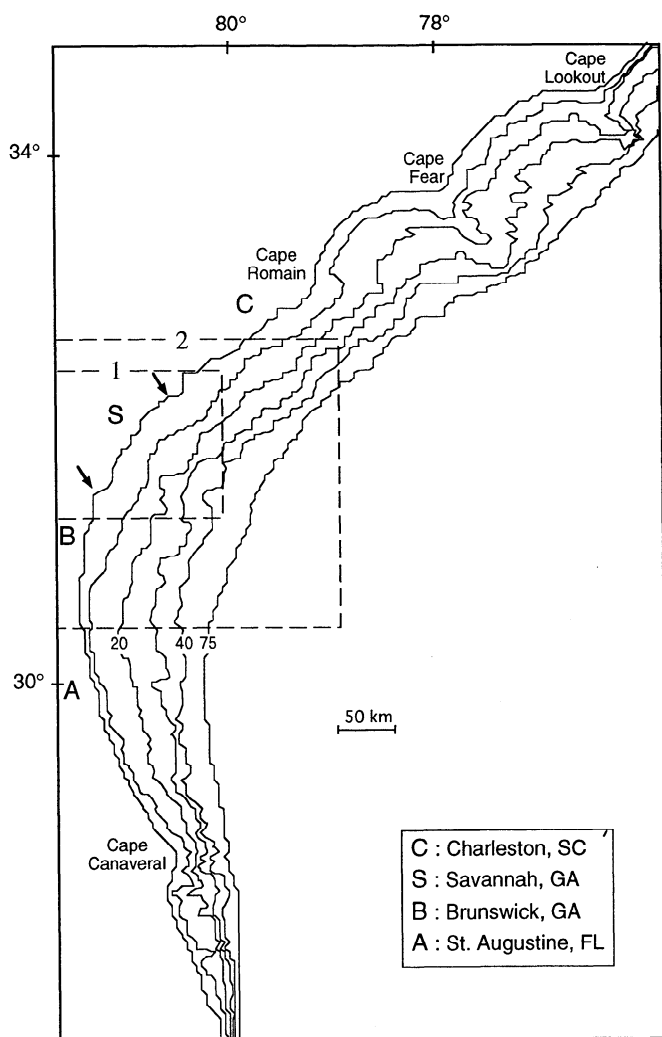


Figure 10. The South Atlantic Bight model domain and subregions 1 and 2 used as domain-enlarged details for the presentation of results.

shore" coordinate system (τ_l, τ_c) that follows isobath orientation. For consistency, the process studies on wind forcing are limited to the shelf area between Brunswick, Georgia, and Charleston, South Carolina, (Figure 10), where the coastline curvature does not alter significantly. We will often use the terms "upwelling-favorable" and "downwelling-favorable" to simply denote positive and negative wind direction, respectively, taken on the rotated coordinate system.

4.2. Point Source Experiments

The freshwater discharge was introduced at the Savannah river mouth (Savannah, Georgia; see Figure 10), and Q was set to $1300 \text{ m}^3 \text{ s}^{-1}$, representing the discharge of one major river.

4.2.1. Experiment 1. The objective is to examine the development of a river plume under impulsive wind stress. A group of 5-day model simulations was undertaken. Constant discharge ($1300 \text{ m}^3 \text{ s}^{-1}$) and constant wind stress (0.5 dyn cm^{-2}) were prescribed at $t=0$, and only the direction of the wind field was altered as follows:

toward (1) the positive and (2) the negative alongshore direction and toward (3) the positive and (4) the negative cross-shore direction. The development of the plume in the absence of wind was also examined. In all experiments the wind stress tended to move the surface plume downwind. As an example, surface salinity fields after 5 days for cases (1) and (2) are shown in Figure 11. For clarity, the velocity fields are plotted at every other grid point and for currents that are larger than 5 cm s^{-1} only. "Northward" wind stress (Figure 11a) led to greater offshore extent of the plume and prevented the development of a southward coastal current. "Southward" wind stress (Figure 11b) restricted offshore movement but enhanced the development of a coastal current immediately south of the discharge site. The stratified area of the shelf was thus limited to a small part of the inner shelf around Savannah. Offshore winds (not shown) also enhanced southward currents in the upper layer of the plume due to superposition of southward Ekman transport. Onshore winds (not shown) resulted in the weakest plume currents and the containment of the plume near the discharge point.

We tabulate the sea surface elevation and upper layer velocity fields along two cross sections: through the river plume at Savannah and outside of the plume region through Charleston, South Carolina (Table 3). In general, the magnitude of the velocities for the inner shelf at Savannah (total depth $H < 20 \text{ m}$) were higher than at the Charleston section due to the stratification around Savannah, hence reduced friction. In the Charleston area the cross-shore distribution of surface properties exhibited a mirror image for positive and negative wind stress, typical of homogeneous conditions. Table 3 (Savannah section) also gives results in the absence of wind stress. Buoyancy was responsible for about a 3 cm increase in coastal elevation and created velocities of 7 cm s^{-1} in the cross-shore u ("eastward") direction and -9 cm s^{-1} in the alongshore v ("southward") direction in the vicinity of the freshwater source.

4.2.2. Experiment 2. The effect of wind stress on a preexisting buoyant plume is studied next. We performed a 20-day model simulation, where the specified forcing was as follows. Buoyancy input only during the first 15 days ($1300 \text{ m}^3 \text{ s}^{-1}$ freshwater discharge at the Savannah River) and both buoyancy and northward wind stress (0.5 dyn cm^{-2}) for the final 5 days. Figure 12a shows the surface salinity field after $t=15$ days. The characteristics of the plume are as expected according to the buoyancy process studies (section 3) for the case of a strong discharge and sloping topography: the low-salinity water extended progressively southward and northward, while the offshore extension was restricted by the topographic slope. A bulge and a coastal current region are also revealed in the superimposed velocity fields. The predominant flow has a strong offshore component within the bulge and a southward component within the coastal current region. Sea level rise was 3.5 cm near the freshwater source and the offshore discharge velocity was 7.5 cm s^{-1} ; the southward coastal current had typical values of about $10\text{--}15 \text{ cm s}^{-1}$.

At the end of the first day of wind forcing ($t=16$ days, not shown) the sea level had dropped to about 0.5 to 1 cm in the vicinity of the source; the u velocity was 5 to 40 cm s^{-1} within the plume and less than 5 cm s^{-1} outside; the v

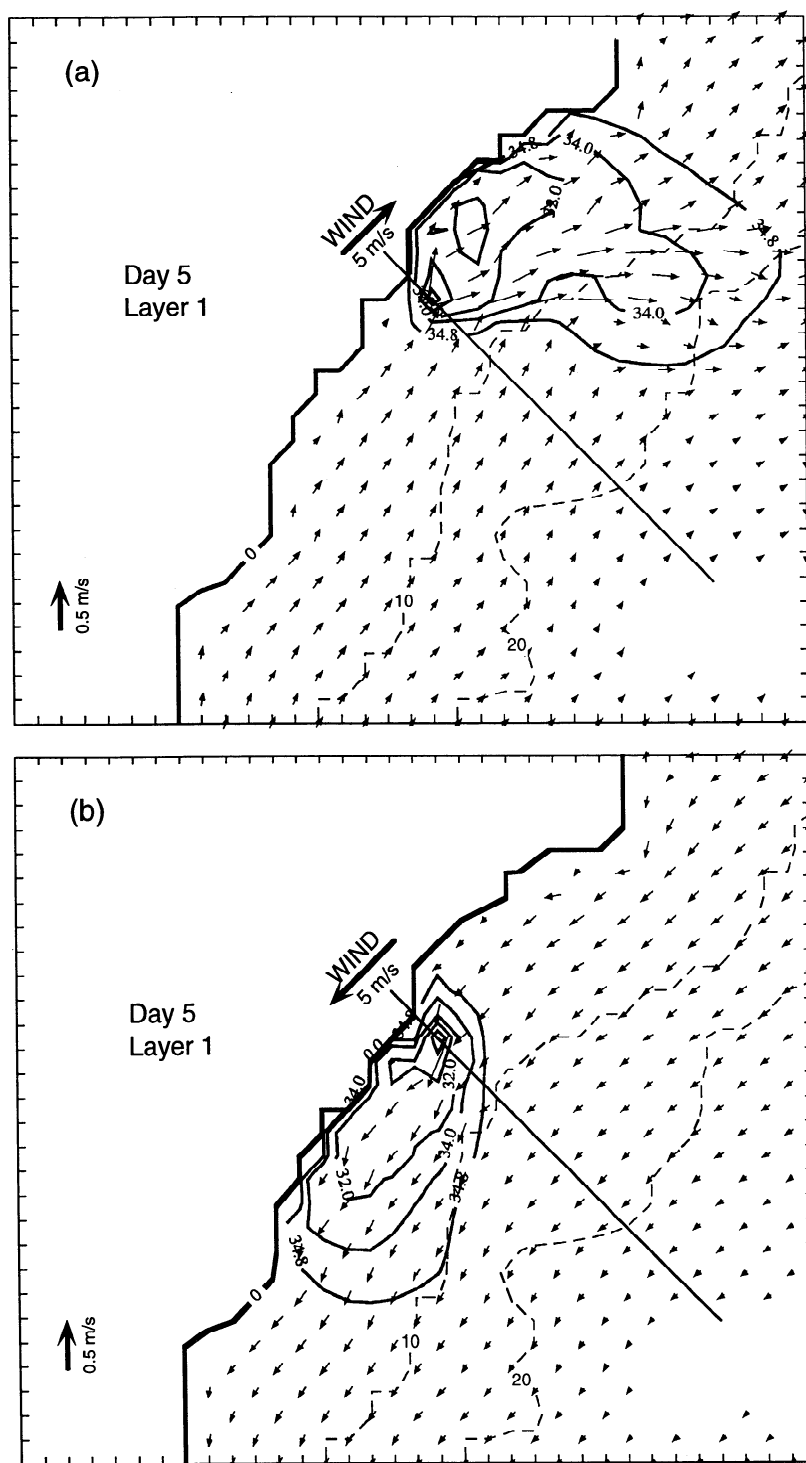


Figure 11. Experiment 1, model-computed surface salinity (contour interval is 2 ppt) and velocity for point source at Savannah and after 5 days of wind stress in the following directions: (a) northward (positive alongshore) and (b) southward (negative alongshore). Salinity contour interval is 5 ppt for $S \leq 32$ ppt. The boundary of the plume is marked by the 34.8 ppt isohaline. Solid lines indicate transect that originates from the Savannah River.

velocity was still negative and up to 10 cm s^{-1} within the plume, while positive and about 1 to 2 cm s^{-1} in the homogeneous areas. The buoyancy-induced response was thus still dominant within the stratified region, featuring surface flow that was nearly opposite to that of the offshore wind-driven region. After 5 days of wind forcing

($t=20$ days, Figure 12b) sea level was negative and velocities were positive everywhere, indicating that the wind forcing dominated over buoyancy in determining the spreading of the low-salinity water. Typical surface values within the plume were an elevation set-down of 10 cm and velocities of 10 to 50 cm s^{-1} . The surface currents were

Table 3. Free Surface Elevation η , Surface Cross-Shore Velocity u , and Surface Alongshore Velocity v During Positive Alongshore $\tau_1 > 0$, Negative Alongshore $\tau_1 < 0$, Offshore $\tau_c > 0$, and Onshore $\tau_c < 0$ Wind Stress and in the Absence of Wind

Depth, m	η , cm					u , cm s ⁻¹					v , cm s ⁻¹				
	$\tau_1 > 0$	$\tau_1 < 0$	$\tau_c > 0$	$\tau_c < 0$	No Wind	$\tau_1 > 0$	$\tau_1 < 0$	$\tau_c > 0$	$\tau_c < 0$	No Wind	$\tau_1 > 0$	$\tau_1 < 0$	$\tau_c > 0$	$\tau_c < 0$	No Wind
<i>Savannah Cross Section</i>															
5	-8.6	10.2	-2.7	8.1	3.1	41.4	-16.4	27.6	4.7	7.1	32.4	-54.9	-38.5	2.6	-9.4
8	-7.3	6.7	-2.6	3.6	0.7	7.0	-8.6	-9.2	-0.1	-7.5	12.2	-7.3	-23.6	3.6	-2.1
14	-5.9	5.7	-2.7	2.6	0.0	5.6	-7.3	-1.1	0.4	0.2	10.2	-7.5	-5.1	4.2	0.9
17	-4.7	4.8	-2.3	2.2	0.0	7.8	-8.3	1.1	-1.2	-0.1	9.6	-7.8	-3.2	3.7	0.1
20	-3.6	3.8	-1.8	1.7	0.0	7.1	-7.7	0.5	-0.5	0.0	6.6	-6.1	-4.8	5.1	0.0
32	-3.0	3.1	-1.6	1.6	0.0	5.9	-6.2	-0.4	0.4	0.0	5.2	-5.1	-3.9	4.0	0.0
40	-2.5	2.6	-1.5	1.5	0.0	3.0	-4.2	-1.4	1.4	0.0	3.8	-4.0	-3.9	4.0	0.0
<i>Charleston Cross Section</i>															
5	-5.8	5.9	-5.2	5.2		14.2	-14.2	9.5	-9.3		13.3	-13.3	-1.0	1.2	
12	-5.0	5.0	-3.0	2.9		10.7	-10.8	2.5	-2.5		6.5	-6.6	-1.9	1.9	
19	-4.1	4.1	-2.2	2.2		9.5	-9.7	-0.1	0.3		5.4	-5.4	-3.4	3.6	
19	-3.3	3.3	-1.9	1.9		10.1	-10.0	0.9	-0.9		5.2	-5.2	-4.5	4.5	
23	-2.4	2.5	-1.6	1.6		10.2	-10.1	1.2	-1.2		4.5	-4.7	-4.5	4.5	
30	-1.6	1.6	-1.5	1.5		9.7	-9.1	0.6	-0.6		4.8	-4.8	-4.5	4.5	
40	-0.8	0.8	-1.3	1.3		8.7	-8.1	1.7	-1.7		3.6	-3.5	-4.6	4.4	

strongest within the stratified plume in the northward and eastward directions and contributed to the offshore spread of low-salinity water northeast of the source. The wind stress eliminated the southward propagation of the plume and the buoyancy-driven coastal current. The offshore extent of the plume was greatly enhanced on the surface, where it reached as far as the midshelf (30 m isobath). Near-bottom flow (not shown) was weak and generally downwind, with the exception of the strongly stratified plume region, where it was directed onshore to compensate the offshore surface currents.

The above experiment was repeated for different combinations of buoyancy and wind stress inputs. The results were very similar qualitatively, with the relative magnitude of the two forcings dictating the duration of the adjustment phase. Thus, for moderate to strong winds (5–10 m s⁻¹) it took 0.5 to 5 days (depending on the plume's "strength") to reverse the buoyancy-driven southward current and follow the opposing wind stress. Light winds (less than 5 m s⁻¹) had a similar effect on a weak plume ($Q \approx 200\text{--}500 \text{ m}^3 \text{ s}^{-1}$) but a minimal effect on a strong plume ($Q \approx 1000\text{--}2000 \text{ m}^3 \text{ s}^{-1}$). A pronounced, offshore, jetlike flow was present when both buoyancy and wind forcings were increased. We also examined the role of topography in the development and propagation of the plume in the absence of wind. The results were similar to the process studies in section 3.2.

4.3. Line Source Experiments

We assume that the plumes from several SAB rivers tend to blend and form a low-salinity band along the coast. The freshwater discharge was set to a total of $4000 \text{ m}^3 \text{ s}^{-1}$ and was distributed equally among point sources all along the coastline between the two arrows in Figure 10 (model

subregion 2). The line source was about 100 km long and was centered on Savannah. The model was run for 5 days without wind forcing in order to develop coastal stratification that would approximate the result from the blending of several river plumes. Integration was continued with different wind forcings.

4.3.1. Experiment 3. We first study the development of the coastal low-salinity band in the absence of wind forcing. After 5 days of development the plume was bounded by the 10-m isobath, the coastal current had an average velocity of 10 cm s^{-1} and the plume extended 35 km south of the source's tail. Since the first 5 days of simulation for all subsequent experiments were performed with buoyancy forcing only, this field can be viewed as an initial condition for the line source study. Figure 13a shows the results for $t=25$ days. The bulge at the source head and the sharp turning of the isohalines at the "nose" of the bulge toward the coast are reminiscent of the point source plume and coastal current system that was studied in section 3. The width of the coastal current south of the head bulge has reached the 15-m isobath. The rate at which the plume expanded south of the source tail was about 6 km d^{-1} . The calculated velocity field (not shown) was anticyclonic in the bulge, turned cyclonically south of the bulge, and then exhibited a slight meandering in the coastal current.

4.3.2. Experiment 4. The 5 days of integration with the line source were followed by 20 days of integration with 0.5 dyn cm^{-2} southward wind stress forcing, typical of a wind event during fall (Figure 13b). Cross-shore development was considerably diminished, and the plume occupied the shallowest part of the inner shelf bounded by the 10-m isobath. Northward spreading at the head was totally eliminated, and the southward

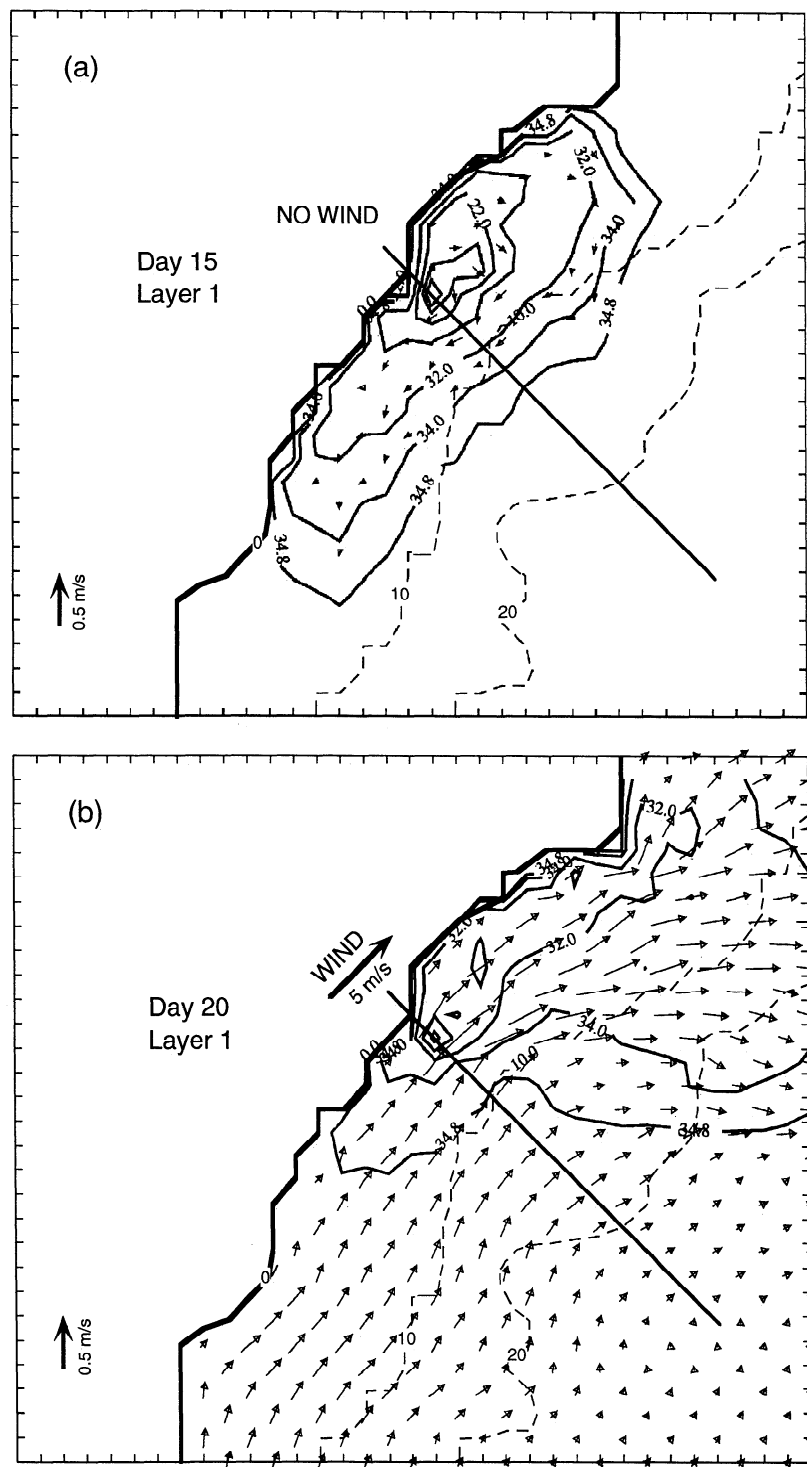


Figure 12. Experiment 2, model-computed surface salinity for (a) day 15 (no wind) and (b) day 20 (northward wind). Salinity contours are marked as in Figure 11.

displacement was about twice that of the zero wind stress experiment 3.

4.3.3. Experiment 5. We examine the influence of wind field "relaxation" periods on the riverine plume. The first 15 days were identical to experiment 4 (5 days of no wind stress followed by 10 days of southward wind). The wind was then turned off, and the integration was continued

for 10 more days. After 5 days of no wind the plume showed significant offshore displacement and a bulge started to form at the source head. After 10 more days of no wind (Figure 13c) the plume had reached almost as far offshore as during the 25-day of the no-wind experiment 3 (Figure 13a). The calculated velocity field (not shown) was also similar to that in experiment 3, anticyclonic flow

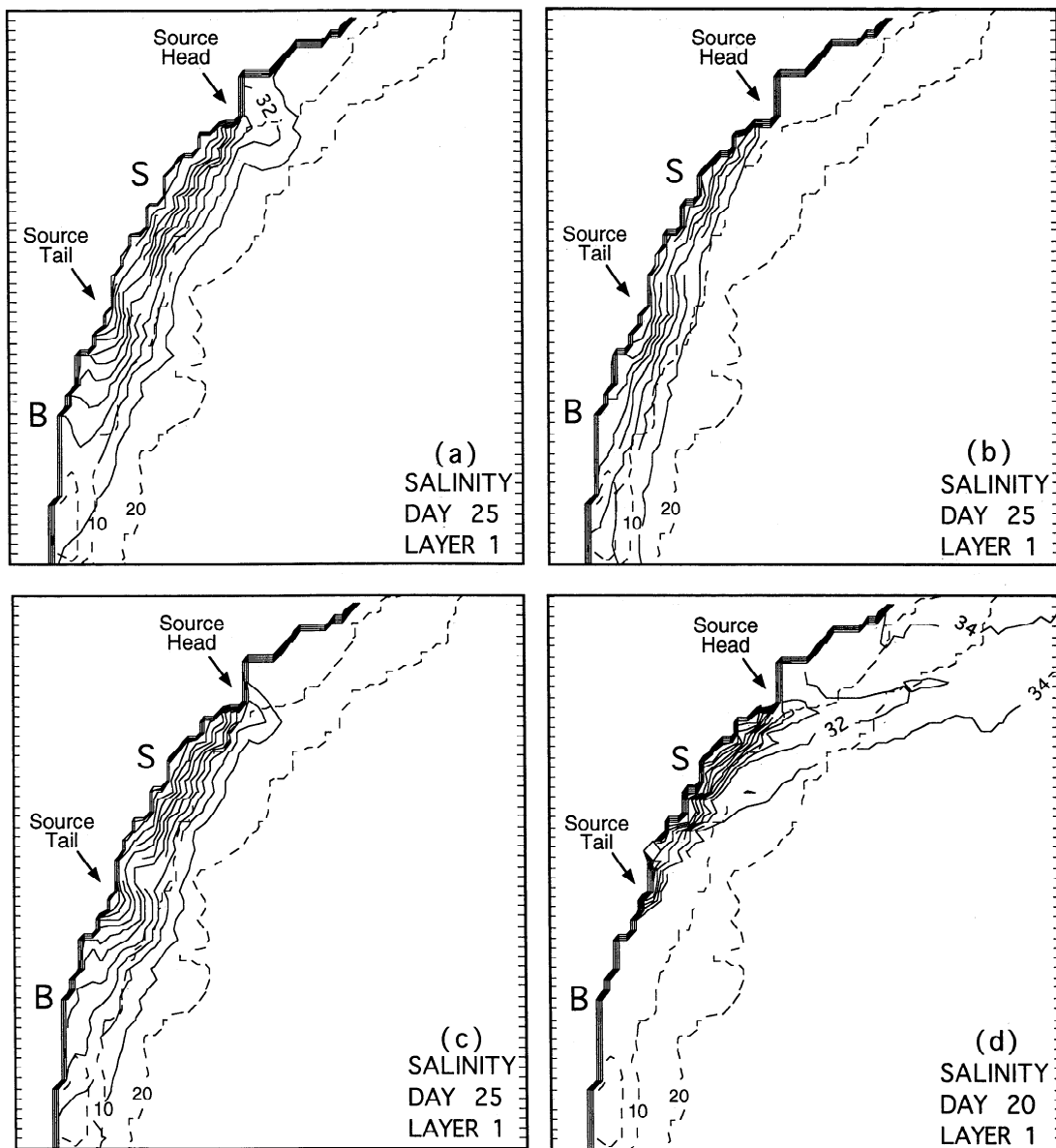


Figure 13. Model-computed surface salinity (contour interval is 2 ppt) for line source of freshwater. All simulations start with 5 days of no wind, (a) Experiment 3, no wind, day 25, (b) Experiment 4, 20 days of southward wind, day 25, (c) Experiment 5, 10 days of no wind following a southward wind event, day 25, (d) Experiment 6, 15 days of northward wind, day 20. The boundary of the plume is marked by the 34 ppt isohaline. The line source is specified between the "head" and "tail" arrows; S is Savannah, Georgia; B is Brunswick, Georgia.

within the bulge and meandering southward current both along the line source and farther downstream.

4.3.4. Experiment 6. When a 0.5 dyn cm^{-2} northward wind stress was applied to the plume that evolved after 5 days of constant discharge, the offshore extent of the plume increased dramatically in the surface layer. The plume expanded to the edge of the inner shelf (20-m isobath) at about 5 days and showed a strong northeastward propagation by $t=20$ days (Figure 13d). The strongest offshore displacement was observed for the outer part of the plume ($S \geq 32$ ppt, as in the point source experiments) and near the source head, where the salinity gradients were largest due to the northward advection of

low-salinity water from each individual source. The formation of "lenses" of low-salinity water was also observed. Although the lenses tended to mix with the ambient waters within a day or so, they suggest a possible mechanism for the removal of coastal low-salinity waters. As in the point source experiments, the flow in the deeper layers (not shown) exhibited much smaller tendency for offshore movement.

4.4. Discussion

The point source experiments showed the basic response of shelf waters to wind stress in the presence or absence of stratification (areas influenced by the plume or far from it,

respectively). In shelf areas that remained homogeneous, coastal elevation rose (fell) for negative (positive) wind stress and the velocities were almost uniform across the shelf with the exception of higher values at the coast. Within the stratified shelf area the coastal elevation setup was higher than the set-down, as the former was due to the combined effect of volume discharge and negative wind stress, while the latter was due to positive wind stress only. When upwelling-favorable wind stress was applied on a preexisting plume, the near-surface flow was reversed from the buoyancy-driven southward direction to a downwind acceleration near the coast and an offshore jetlike flow farther seaward. The cause of this structure is the enhancement of offshore Ekman transport in the stratified portion of the plume seaward of the coastal zone, where the "coastal constraint" (no cross-shore transport in the proximity of the coast) leads to acceleration of the flow downwind [Csanady, 1982]. The offshore surface transport created onshore bottom transport (adjustment drift), which caused the northward advection of the deeper parts of the plume.

When a line source was employed, the formation and growth of the bulge were due to the coastal elevation gradient at the first source node. The freshwater discharge generated an offshore (negative in the x -direction) pressure gradient at each individual source node. The discharge at the first (head) and last (tail) source nodes also caused a pronounced alongshore pressure gradient (negative and positive in the y direction, respectively). The alongshore pressure gradient at the tail produced the southward flowing coastal current, while the gradient at the head generated a buoyant plume in a manner similar to that of a single point source.

In general, upwelling-favorable wind stress relaxed the buoyancy-generated coastal front, while downwelling-favorable wind stress made it steeper. Offshore removal of riverine waters is thus promoted by the former. This result agrees with previous numerical studies, as well as observations (see section 1). Our findings further point out that the enhancement exists not only during upwelling-favorable winds, but also during relaxation of the wind field after a period of downwelling-favorable winds. The latter was documented during a fall experiment in the SAB, when after a long period of downwelling-favorable winds and a subsequent sudden wind relaxation, the width of the nearshore low-salinity band increased substantially [Blanton *et al.*, 1994]. Our experiments also suggest that it is possible to have a southward buoyancy-driven current near the coast, while offshore wind-driven flow is northward, during periods of strong river runoff and light upwelling-favorable winds. This seemed to be the case during the spring of 1985 in the SAB (SPREX field study), when measured inner shelf currents presented a similar feature [Blanton *et al.*, 1989]. We speculate that the presence of a buoyancy-supplying source during upwelling-favorable winds may suppress the tendency for downwind acceleration of nearshore waters. The situation is different during homogeneous conditions, when the nearshore waters respond almost in phase with the wind, several hours faster than the offshore shelf waters [Lee *et al.*, 1985; Kourafalou *et al.*, this issue].

5. Summary and Conclusions

The development and evolution of a midlatitude buoyant plume that results from freshwater river discharge to an ocean basin were studied. The results presented herein were the product of three-dimensional numerical simulations based on two major forcing mechanisms: buoyancy and wind stress.

In the absence of wind stress, rotation and nonlinearity were found important. A plume classification scheme based on a bulk Richardson number Ri was derived. For $Ri^{1/3}$ greater (less) than 1 the plume is supercritical (subcritical). Supercritical plume leads to expansive bulge and encourages coastal current meandering. The meandering is caused by a baroclinic instability process and is enhanced with increased buoyancy and reduced or eliminated with increased mixing. For a given discharge, subcritical plumes are produced by large mixing and/or shallow water depths. The introduction of even moderate bottom slope elongates the plume within a narrow nearshore strip and reduces its offshore expansion.

When the buoyancy-driven southward flow is forced by opposing wind stress, the degree of coastal current reversal and the timescale of this flow adjustment are determined by the relative magnitude of wind and buoyancy forcings. Thus, while light winds (less than 5 m s^{-1}) have a minimal effect on strong plumes, moderate to strong winds ($5\text{--}10 \text{ m s}^{-1}$) may fully reverse the buoyancy-driven current within a few hours to a few days (depending on the plume's "strength"). On the other hand, the established stratification in the plume region enhances offshore Ekman transport. Intense offshore advection of the coastal low-salinity waters may thus take place during high river runoff and upwelling-favorable winds.

Within the shelf area that is influenced by a single river (point source), the wind-driven flow exhibits significant spatial variability. Strong seaward flow forms near the source, in contrast to the surrounding downwind flow, when wind stress is upwelling-favorable. When many rivers are close enough to form a line source, offshore transport during upwelling-favorable winds will be most pronounced at the head of the source. During downwelling-favorable wind stress the cross-shore transport of coastal low-salinity water will be restricted. However, "relaxation" of the wind field after strong events of downwelling-favorable winds will again favor offshore removal of plume waters that had been previously confined near the coast.

During a numerical simulation that employs realistic (time and space varying) wind stress and freshwater discharge forcings, the following implications are derived from the conclusions above. The shelf response to the combined input of river runoff and wind stress will be determined by the relative strength of the outflow, the river's location, and the magnitude, direction, and duration of the wind stress. The seasonal variability of the two forcings will therefore influence the removal of low-salinity waters from the inner shelf. For the SAB continental shelf the hypothesis of strongest removal during springtime is expected to hold, due to the combination of highest runoff and mean northeastward

wind stress that characterizes the spring season. Since several SAB rivers are close to each other, a line source behavior should be generally valid. However, the employment of realistic discharge and wind stress values will probably encourage the point source behavior, as differences in local conditions become important. During wind reversals and during wind field relaxation periods (which could allow even moderate plumes to strengthen), it may be possible to have opposite alongshore flows within the inner shelf and in the vicinity of rivers. This is due to two reasons. First, the time lag in the response of nearshore and offshore shelf regions to wind stress can cause different direction in the wind-driven shelf flows, as the nearshore region would respond faster to a shift in wind direction. On the other hand, a strong buoyancy-related southward coastal current may prevail against opposite wind-driven shelf flow. In addition, the transport of riverine waters will be influenced by topography. The role of bottom stress should be addressed further, as it is particularly important in the shallow depths, where the establishment of the river plume takes place. A careful parameterization of bottom stress for a realistic application should include the effect of tides.

Appendix: Model Implementation of River Discharge

Since we will only consider a source of freshwater, the source mass of salt is zero and the constituent mass transport equations are unchanged. In our approach the momentum associated with river discharge is assumed negligible at the model grid resolution and thus the source contribution in the momentum equations is also ignored. The river discharge is $Q(t)$ with units $[L^3T^{-1}]$ and is assumed distributed over a model horizontal area A . For instance, point source simulations adopt the area of one grid cell $(\Delta x, \Delta y)$ for A . The connection between the sigma σ and the cartesian coordinate systems is

$$\langle x^*, y^*, \sigma, t^* \rangle = \left\langle x, y, \frac{z - \eta}{D}, t \right\rangle. \quad (16)$$

We are then left with the following modifications to the continuity equations.

Taking $D = h + \eta$, where h is depth, η is surface elevation, and q is distribution of Q within the area A (q has units of velocity), the two-dimensional continuity equation (external mode) includes a source term.

$$\eta_t + (Du)_x + (Dv)_y = q(x, y, t) \quad (17)$$

Analogously, the three-dimensional continuity equation (internal mode) is:

$$\eta_t^* + (Du)_x^* + (Dv)_y^* = q^*(x^*, y^*, \sigma, t^*) \quad (18)$$

For compatibility, the external and internal source functions are related as follows:

$$Q = \int_A q dA = \int_A \int_{-1}^0 q^* d\sigma dA. \quad (19)$$

Assuming that q is discharged on the top layer, being constant within this layer and zero outside of it, we have:

$$\int_{-1}^0 q^* d\sigma = q^* \Delta\sigma \quad (20)$$

which gives

$$q = \frac{Q}{A} = \int_{-1}^0 q^* d\sigma \quad (21)$$

and therefore:

$$q^* = \frac{Q}{A\Delta\sigma}. \quad (22)$$

Acknowledgments. We thank Rainer Bleck and Linda Smith for many helpful discussions concerning NCAR computing and Jean Carpenter for drafting assistance. We greatly appreciate the computer time extended by NCAR for model runs on the CRAY Y-MP. Funding for this work has been supplied by U. S. Department of Energy contract DE-FG05-85ER60355 and National Science Foundation grants OCE-88-12745 and OCE-89-11859.

References

- Blanton J.O., L.-Y. Oey, J. Amft, and T.N. Lee, Advection of momentum and buoyancy in a coastal frontal zone, *J. Phys. Oceanogr.*, **19**, 98-115, 1989.
- Blanton, J.O., F. Werner, C. Kim, L.P. Atkinson, T. N. Lee, and D. Savidge, Transport and fate of low-density water in a coastal frontal zone, *Cont. Shelf Res.*, **14**(4), 401-427, 1994.
- Blumberg, A.F., and G.L. Mellor, Diagnostic and prognostic numerical circulation studies of the South Atlantic Bight, *J. Geophys. Res.*, **88**(C8), 4579-4592, 1983.
- Chao, S.-Y., Wind-driven motion near inner shelf fronts, *J. Geophys. Res.*, **92**(C4), 3849-3860, 1987.
- Chao, S.-Y., River-forced estuarine plumes, *J. Phys. Oceanogr.*, **18**, 72-88, 1988.
- Chao, S.-Y., and W.C. Boicourt, Onset of estuarine plumes, *J. Phys. Oceanogr.*, **16**, 2137-2149, 1986.
- Csanady, G.T., Mean circulation in shallow seas, *J. Phys. Oceanogr.*, **81**, 5389-5399, 1976.
- Csanady, G.T., *Circulation in the Coastal Ocean*, 279 pp, D. Reidel, Norwell, Mass., 1982.
- Csanady, G.T., Circulation induced by river inflow in well mixed water over a sloping continental shelf, *J. Phys. Oceanogr.*, **14**, 1703-1711, 1984.
- Fischer, H.B., E.J. List, R.C.Y. Koh, J. Imberger, and N.H. Brooks, *Mixing in Inland and Coastal Waters*, 477 pp., Academic, San Diego, Calif., 1979.
- Garvine, R.W., Frontal jump conditions for models of shallow, buoyant surface plume hydrodynamics in coastal waters, *Tellus*, **33**, 301-312, 1981.
- Garvine, R.W., Estuary plumes and fronts in shelf waters: A layer model, *J. Phys. Oceanogr.*, **17**, 1877-1896, 1987.
- Gill, A.E., The hydraulics of rotating-channel flow, *J. Fluid Mech.*, **80**, 641-671, 1977.
- Hansen, D.V. and M. Rattray, New dimensions in estuary classification, *Limnol. Oceanogr.*, **11**(3), 319-325, 1965.
- Hickey, B.M., and P. Hamilton, A spin-up model as a diagnostic tool for interpretation of current and density measurements on the continental shelf of the Pacific Northwest, *J. Phys. Oceanogr.*, **10**, 10-24, 1980.
- Ikeda, M., Coastal flows driven by a local density flux, *J. Geophys. Res.*, **89**(C5), 8008-8016, 1984.

- Kao, T.W., The dynamics of small scale fronts, I, Shelf water structure due to freshwater discharge, *J. Phys. Oceanogr.*, **11**, 1215-1223, 1981.
- Kao, T.W., C. Park, and H.-P. Pao, Buoyant surface discharge and small-scale oceanic fronts: A numerical study, *J. Geophys. Res.*, **82**(12), 1747-1752, 1977.
- Kourafalou, V.H., Continental shelf response to freshwater input from rivers: A 3-D model study and applications, Ph.D. thesis, 218 pp., Univ. of Miami, Miami, Fla., 1993.
- Kourafalou, V.H., T.N. Lee, L.-Y. Oey, and J.D. Wang, The fate of river discharge on the continental shelf, 2, Transport of coastal low-salinity waters under realistic wind and tidal forcing, *J. Geophys. Res.*, This issue.
- Lee, T.N., V. Kourafalou, J.D. Wang, W.J. Ho, J.O. Blanton, and L.P. Atkinson, Shelf circulation from Cape Canaveral to Cape Fear during winter, in *Oceanography of the Southeastern U.S. Continental Shelf*, Coastal Estuarine Sci. Ser., Vol. 2, edited by L.P. Atkinson, D.W. Menzel, and K.A. Bush, pp. 33-62, AGU, Washington, D.C., 1985.
- Mamayev, O.I., *Temperature-Salinity Analysis of World Ocean Waters*, Elsevier, New York, 1975.
- McClimans, T.A., Estuarine fronts and river plumes, in *Physical Processes in Estuaries*, edited by J. Dronkers and W. van Leussen, pp. 55-69, Springer-Verlag, New York, 1986.
- Mellor, G.L., and T. Yamada, Development of a turbulence closure model for geophysical fluid problems, *Rev. Geophys.* **20**(C4), 851-875, 1982.
- Oey, L.Y., and P. Chen, A model simulation of circulation in the northeast Atlantic shelves and seas, *J. Geophys. Res.*, **97**, 20,087-20,115, 1992.
- Oey, L.-Y., and G.L. Mellor, Subtidal variability of estuarine outflow, plume and coastal current: A model study, *J. Phys. Oceanogr.*, **23**, 164-171, 1993.
- Orlanski, I., A simple boundary condition for unbounded hyperbolic flows, *J. Comput. Phys.*, **21**, 251-269, 1976.
- Wang, D.P., Mutual intrusion of a gravity current and density front formation, *J. Phys. Oceanogr.*, **14**, 1191-1199, 1984.
- V. H. Kourafalou, Consiglio Nazionale delle Ricerche, Istituto per lo Studio delle Metodologie Geofisiche Ambientali, 770 Via Emilia Est Modena, 41100 Italy . (e-mail: villy@eletra.bo.cnr.it)
- T. N. Lee, Rosenstiel School of Marine and Atmospheric Science, University of Miami, Division of Meteorology and Physical Oceanography, Miami, Florida 33149. (e-mail: tlee@rsmas.miami.edu)
- L.-Y. Oey, Atmospheric and Oceanic Science Program, Princeton University, Sayre Hall, Forrestal Campus, Princeton, New Jersey 08544. (e-mail: lyo@kuroshio.princeton.edu)
- J. D. Wang, Rosenstiel School of Marine and Atmospheric Science, University of Miami, Division of Applied Marine Physics, Miami, Florida 33149. (jwang@rsmas.miami.edu)

(Received October 13, 1994; revised June 21, 1995;
accepted September 28, 1995.)